



Carbon nitride modified hexagonal boron nitride interface as highly efficient blue LED light-driven photocatalyst

Tiansheng Chen^a, Qianxin Zhang^a, Zhijie Xie^a, Cuiwen Tan^a, Ping Chen^b, Yongqin Zeng^a, Fengliang Wang^a, Haijin Liu^c, Yang Liu^d, Guoguang Liu^{a,*}, Wenying Lv^{a,*}

^a School of Environmental Science and Engineering, Institute of Environmental Health and Pollution Control, Guangdong University of Technology, Guangzhou, 510006, China

^b School of Environment, Tsinghua University, Beijing 100084, China

^c School of Environment, Henan Normal University, Key Laboratory for Yellow River and Huaihe River Water Environment and Pollution Control, Xinxiang 453007, China

^d Faculty of Environmental & Biological Engineering, Guangdong University of Petrochemical Technology, Maoming 525000, China



ARTICLE INFO

Keywords:

Carbon nitride modified hexagonal boron nitride
Blue LED light
Enrofloxacin
Degradation pathways

ABSTRACT

Hexagonal boron nitride (BN) nanomaterials that possess an extensive specific surface area, negatively charged properties, high thermal conductivity, and excellent chemical characteristics, have significant advantages for water purification and energy storage. They are typically considered as potential catalysts due to their wide tunable bandgap. Here, carbon nitride (CN) modified BN (CMBN), which facilitated the formation of new C–N–B bonds, was successfully synthesized using a facile hydrothermal-calcination synthesis strategy. Such highly active bonds made the photocatalyst responsive to a wider range of wavelengths (e.g., ultraviolet to visible blue light), while significantly enhancing photocatalytic activity toward the degradation of enrofloxacin (ENFX). A 3-CMBN sample exhibited 39.3 times, and 2.4 times, higher photocatalytic properties than that of pristine BN and CN, respectively. The remarkable response of 5, 5-dimethyl-1-pyrrolidone-*N*-oxyl (DMPOX) was investigated through electron spin resonance spectroscopy (EPR) with 3-CMBN, which indicated higher oxidability than BN and CN under blue LED irradiation. Reactive species scavenging experiments revealed that the photodegradation of ENFX was dominated by electron holes and O₂^{·-}. Moreover, the byproducts of ENFX were detected by HPLC-Q-TOF and GC-MS, probable pathways toward these byproducts were deduced, and repeated tests confirmed good stability. These results provided a new strategy to guide the enhanced design of advanced photocatalysts with active chemical bonding species, which can be applied to environmental remediation.

1. Introduction

At this juncture, it is of great significance to develop effective multifarious strategic solutions to resolve critical global scale issues, such as continually worsening environmental pollution, while increasing the developmental capacities for clean energy supplies. In recent years, graphene and graphite-like materials have garnered widespread attention due to their unique structures and electronic properties [1–4].

Hexagonal boron nitride (BN) comprises a type of two-dimensional metal-free material with a structure that is analogous to graphite. It shares several common properties with graphite, including anisotropy, basal plane perpendicularity, high mechanical strength, thermal conductivity, and good lubricity [5]. Unlike graphite, the unique structural

features of BN's interlayer stacking pattern endows it with many additional electrical, optical, and chemical characteristics [6,7]. These attributes make BN very useful for myriad applications. BN based catalytic materials have demonstrated excellent photocatalytic activities. Hence, they may be employed for many photocatalytic applications such as hydrogen production, the oxidation of organic pollutants, and redox or selective oxidative dehydrogenation [8,9]. Conversely, since the bandgap of h-BN is relatively large (ranging from ~3.98 eV and 6 eV), it may only absorb light at wavelengths of < 310 nm in the solar spectrum, which greatly limits its utilization of light [10,11]. BN is often combined toward the development of enhanced materials with improved photocatalytic properties for the degradation of organic compounds. Among the results previously obtained from photocatalysis investigations, BN-modified catalysts that contain both metallic and

* Corresponding authors at: School of Environmental Science and Engineering, Guangdong University of Technology, No. 100 Waihuan Xi Road, Guangzhou Higher Education Mega Center, Guangzhou, 510006, China.

E-mail addresses: liugg61@163.com (G. Liu), lvwy612@163.com (W. Lv).

nonmetallic compounds may greatly improve the properties of semiconductor materials, such as TiO₂/BNNT (boron nitride nanosheets) [12], SnO₂/BNMB (boron nitride submicro-boxes) [13], BN/ZnO [14], h-BN/Ag₃PO₄ [15], BN/AgBr [16], BN/WO₃ [17], BN/In₂S₃ [18], and BN/BiOBr [19]. A small amount of BN modification with materials enables the higher separation efficiency of photogenerated electron-hole pairs due to Z-Scheme formation, or the emergence of negatively charged properties.

As a novel and popular 2D graphite nanomaterial, graphitic carbon nitride (CN), possesses a unique electronic energy band structure with excellent chemical stability. CN has an approximate bandgap of 2.7 eV and absorbs light in the solar spectrum at a wavelength of < 460 nm. However, akin to most organic semiconductors, the π -conjugated CN framework is limited by rapid charge recombination [20]. The high recombination rate of photogenerated carriers (electron-hole pairs) and low specific surface area of pure CN, greatly limits its photocatalytic activity [21–24]. Jiang et al. [25] synthesized g-C₃N₄-based composite h-BN/g-C₃N₄ photocatalyst, the holes photoexcited by g-C₃N₄ are transferred due to the electrostatic attraction of trace amount of BN. However, to the best of our knowledge, the mechanisms of enhanced photocatalytic performance of CN modified BN interface have never been studied in depth. To further develop the potential of boron nitride, therefore, understanding the impact of CN modification on the BN interface and the form of interface combination by controlling the amount of CN is a challenge.

Recently, pharmaceutical and personal care products (PPCPs) have raised unprecedented concern as emerging organic contaminants due to their potentially hazardous effects on ambient ecosystems and human health [26,27]. Owing to their extensive anthropogenic use, PPCPs are continuously released into the environment, which has resulted in their being considered as “pseudo-persistent” contaminants [28]. Consequently, it is extremely urgent to evolve effective strategies for the elimination of PPCPs in aquatic systems. Enrofloxacin (ENFX), which comprises a common fluoroquinolone (FQ) antibiotic, is widely employed in human and veterinary medicine [29]. Unfortunately, the majority of ENFX is eventually released into the environment, as it may be only partially metabolized in humans or animals, and is only negligibly biodegradable [30]. Hence, ENFX was selected as a target PPCP for study under blue LED irradiation. In particular, the reaction conditions were very mild without the use of further additives under illumination (450 ± 10 nm, 6 ± 0.1 mW/cm²) by blue light emitting diodes [31]. LED sources generate minimal heat, have high robustness, and exhibit good linearity of emitted light intensity with current. Hence, they are employed for a wide range of applications, including the photocatalytic degradation of environmental contaminants [32–34].

In this work, BN based CN/BN (CMBN) composite photocatalysts were synthesized using a hydrothermal-calcination technique. Since CN itself possesses photocatalytic properties and is rich in carbon, it may also serve as a satisfactory carbon source. Herein, we describe the formation of many new C–N–B chemical bonds with excellent photocatalytic activity at the CN/BN interface, while generating carbon nitride. The physicochemical properties of the as-synthesized photocatalysts were thoroughly characterized by X-ray diffraction (XRD), Raman spectrometry, Fourier infrared spectrometry (FT-IR), scanning electron microscopy (SEM) equipped with energy dispersive X-ray spectrometry (EDS), transmission electron microscopy (TEM), X-ray photoelectron spectroscopy (XPS), UV-vis diffuse reflectance spectra (DRS), etc.. The photocatalytic properties of CMBN on the degradation of enrofloxacin (ENFX) was evaluated under blue-LED irradiation. In addition, the physicochemical properties and enhancement mechanisms of the photocatalytic activities of CMBN were systematically evaluated. Electron spin resonance spectroscopy (EPR) and trapping experiments were conducted to qualitatively detect the roles of reactive species (RSs) during the degradation of ENFX. Potential photo-degradation pathways were proposed based on product identification

by HPLC-Q-TOF, GC–MS, as well as theoretical FED calculations. A mechanism for their highly efficient blue LED light-driven characteristics was also proposed based on experimental results, which showed great potential for the developed carbon nitride modified hexagonal boron nitride photocatalyst, and inspired the further development of the BN-based photocatalytic materials.

2. Experimental

2.1. Materials

Enrofloxacin (ENFX, 98% purity) was obtained from the TCI Reagent Co. Ltd. (China). Melamine (C₃H₆N₆, 99% purity) and boron nitride (BN, 99.8% metals basis, < 100 nm) were purchased from Aladdin (China). HPLC-grade reagents (methanol, acetonitrile, etc.) were obtained from CNW Technologies GmbH (Germany). Analytical grade reagents (4-hydroxy-2, 2, 6, 6-tetramethylpiperidinyloxy, isopropanol, sodium azide, Na₂C₂O₄, etc.) were purchased from Taitan (China) and used without further purification. Deionized (DI) water from a Milli-Q apparatus (Germany) was used for all experiments.

2.2. Preparation and characterization

2.2.1. Preparation of CMBN photocatalyst

The CMBN was prepared via a facile hydrothermal-calcination method. Melamine (3 g) and different weights of BN (0.5, 1, 2, 3, 4, 5 g) were dissolved in a 100 mL alumina crucible with 40 mL ethanol. Subsequently, the mixed suspension was stirred at 80 °C to vaporize the ethanol in a fuming cupboard, followed by ten minutes of ultrasonication. The dry composite powder was then heated to 550 °C for 4 h in an alumina crucible, under a stable heating rate of 3 °C/min.. Once cooled to room temperature, the resulting powder was transferred to an agate mortar and then ground and filtered to collect the final samples. The final samples were tagged as x-CMBN, where x (h represented as 0.5, 1, 2, 3, 4, 5) referred to the weight of the BN. Pure BN underwent the same treatment as above, and CN (g-C₃N₄) was obtained similarly without the addition of BN.

2.2.2. Material characterization

Field emission scanning electron microscopy (SEM) images of these samples (BN, CN, CMBN) were obtained using a JSM-7001 F (Japan) system. Field Emission Transmission Electron Microscopy (TEM, Talos F200S) was also performed. The crystal structure and phase purity of the obtained photocatalysts were characterized by Powder X-ray Diffraction (XRD, BRUKER D8 ADVANCE), equipped with Cu K α radiation ($\lambda = 0.15418$ nm) in the 2 θ range, of from 5–90° at a scanning rate of 8°/min.. X-ray photoelectron spectroscopy (XPS), which was performed using Mg-K α radiation as the excitation source, was equipped with a PHI Quanta 2 \times . UV-vis diffuse reflectance spectra (UV-vis DRS) were identified using a UV2450 UV-vis spectrophotometer (Shimadzu) at room temperature. Fourier transform infrared spectra (FT-IR) were acquired using a Nicolet 6700 spectrometer (Thermo Fisher, USA) with testing wavelengths in the range of from 4000 cm⁻¹ to 400 cm⁻¹. All Raman spectra were measured using a LabRAM HR800 (Horiba Jobin Yvon), which was equipped with a 325 nm He-Cd laser in the range of from 200–4500 cm⁻¹. Brunauer-Emmett-Teller (BET) was employed to measure the specific surface areas of the photocatalysts, which were characterized by N₂ adsorption-desorption at -196°C using an Autosorb-IQ (USA) instrument. The TOC removal ratio was detected by TOC-V CPH. Eco Ion Chromatography (Eco, Metrohm, Switzerland) was performed to detect the photocatalytic degradation of IC. Photoluminescence (PL) spectra were obtained using a FLS980 Series Fluorescence Spectrometer (UK). The photocurrents and electrochemical impedance spectroscopy of the samples were attained using an Electrochemical Workstation (Multi Autolab/204, Metrohm), which was equipped with a standard three-

electrode cell under blue-LED irradiation. An Agilent Technologies liquid chromatograph (6200 series) equipped with a tandem mass spectrometer (Agilent Technologies 6500 series Accurate Mass Quadrupole Time-of-Flight) (HPLC-Q-TOF) and GC/MS (Agilent 7890B-5977B) was carried out to detect the intermediate products, with the details of the analytical methods displayed in Text S1.

2.3. Photocatalytic performance tests

2.3.1. Photocatalytic experiments and analytical method

The photocatalytic activities of the as-prepared samples were evaluated via the photocatalytic degradation of ENFX under blue LED irradiation. The photocatalytic experiments were carried out using a custom fabricated photocatalytic reactor (Scheme S1, Supporting Information), which was equipped with a 100 mL quartz beaker as the reaction vessel, that was illuminated by blue LED lamps (emitting 450 ± 10 nm) with an optical power density of 6 ± 0.1 mW/cm² as the excitation light source, under constant simultaneous magnetic stirring. Typically, 50 mg of the sample was introduced into 50 mL of an 8 mg/L ENFX aqueous solution in a 100 mL quartz beaker. Subsequently, the mixed solution was ultrasonically treated for 1 h and magnetically stirred for 30 min. in the dark to attain adsorption-desorption equilibrium for the ENFX on the photocatalyst prior to the photocatalytic reaction under blue LED irradiation. During the experiments, a 1.0 mL volume of mixed solution was extracted from the reaction vessel at predetermined time intervals and filtered with a 0.22 μ m Millipore filter for the removal of the photocatalyst. The resulting ENFX in solution was detected via high performance liquid chromatography (HPLC). The details of the HPLC detection method are shown in the Text 2.

2.3.2. Determination of RSs during photocatalytic degradation

Radical scavenging experiments were conducted to detect the reactive species (RSs) that were generated during the ENFX photodegradation process. Herein, 1.0 mM 4-hydroxy-2,2,6,6-tetramethylpiperidinyloxy (TEMPO) was employed as a superoxide iron radical ($O_2^{\cdot-}$) scavenger, 10 mM isopropanol (IPA) as hydroxyl radical ($\cdot OH$) scavenger, 75 mM sodium azide (NaN_3) as a singlet oxygen (1O_2) scavenger, and 10 mM sodium oxalate ($Na_2C_2O_4$) as photogenerated hole (h^+) scavenger.

To directly analyze the RSs, electron spin resonance spectroscopy (EPR) spectra were identified using a Bruker JES FA200 (Japan), where 0.05 g/L catalyst and 50 mM DMPO were combined with water to create a suspension. The RSs were detected using a spectrometer following irradiation with visible light to obtain the DMPO- $O_2^{\cdot-}$ and DMPO-OH EPR signals at three different time intervals.

2.4. Theoretical calculation

A hybrid density functional B3LYP/6-311G + (d, p) was implemented in molecular orbital calculations and stationary point geometries. The optimized structure and atomic numbering of enrofloxacin were displayed through the Gaussian 09 program in Fig S1. The highest occupied molecular orbital (HOMO) was calculated, as were the lowest unoccupied molecular orbital (LUMO) and frontier electron densities (FEDs). Therefore, based on the $FED_{HOMO}^2 + FED_{LUMO}^2$ values and point charges, it was possible to predict the reaction sites that were attacked by h^+ , OH , and $O_2^{\cdot-}$.

3. Result and discussions

3.1. Characterizations of 3-CMBN

The crystalline structure and phase purity of materials were determined by XRD characterization, as shown in Fig. 1. Two obvious characteristic peaks of CN may be observed at 13.1° and 27.4°

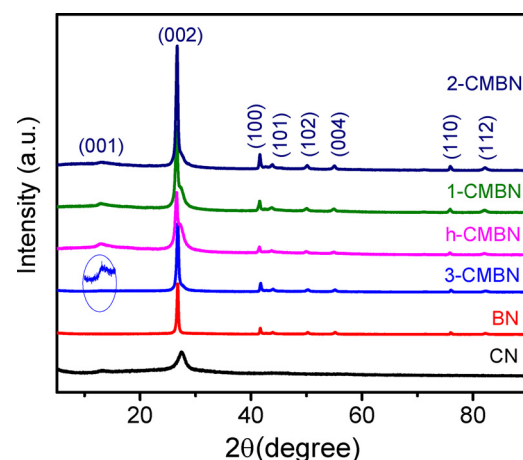


Fig. 1. XRD patterns of different samples.

according to JCPDS Card No. 87-1526, which were attributable to the (001) and (002) planes, respectively. The (001) plane corresponded to the characteristic interlayer stacking structure of aromatic segments [35]. The characteristic (002) plane peak was in accordance with a previous report on graphite-like C_3N_4 [36]. Without melamine carbon, BN revealed two primary characteristic XRD peaks at 26.8° and 41.6° due to the (002) and (100) planes of the graphitic structure of BN, respectively, according to JCPDS card No. 34-0421 [37]. With CN, all the samples featured XRD peaks that were similar to those of BN. Meanwhile, the diffraction peak at 13.1° could be observed via the high resolution XRD spectra of 3-CMBN, which could be ascribed to traces of CN. Furthermore, no other characteristic impurity peaks could be observed, which indicated that high purity crystalline phases were maintained during the synthesis process, whereby the morphologies and crystalline forms of the photocatalysts synthesized primarily with BN were not altered.

The N_2 adsorption-desorption isotherms of the BN, CN, and CMBN samples are depicted in Figs. 2 and S1. As can be seen, the BN and 3-CMBN revealed similar surface features. A type II isotherm with a hysteresis loop was obtained in both BN and 3-CMBN, which revealed narrowly distributed mesoporous structures [38]. Calculations using BET and BJH models indicated that the 3-CMBN, respectively, gave a lower specific surface area of $18.1\text{ m}^2\text{ g}^{-1}$ and a smaller pore volume $0.042\text{ cm}^3\text{ g}^{-1}$ than did BN. This phenomenon further validated the notion that the CN grew on the surfaces of the BN nanoparticles.

To directly confirm the morphologies of the as-prepared samples, they were characterized by SEM. The SEM image in Fig. 3a reveals the

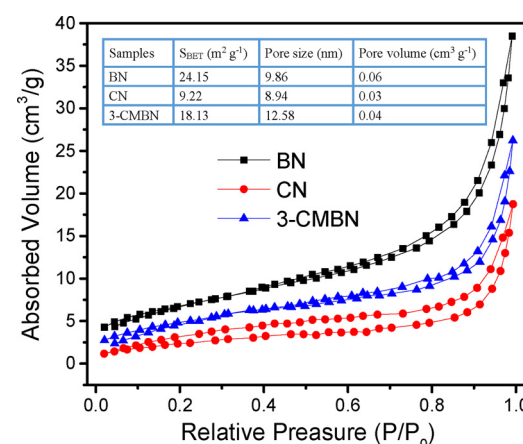


Fig. 2. N_2 adsorption-desorption isotherms, inset: BET surface areas, pore size and pore volumes of the as-prepared samples.

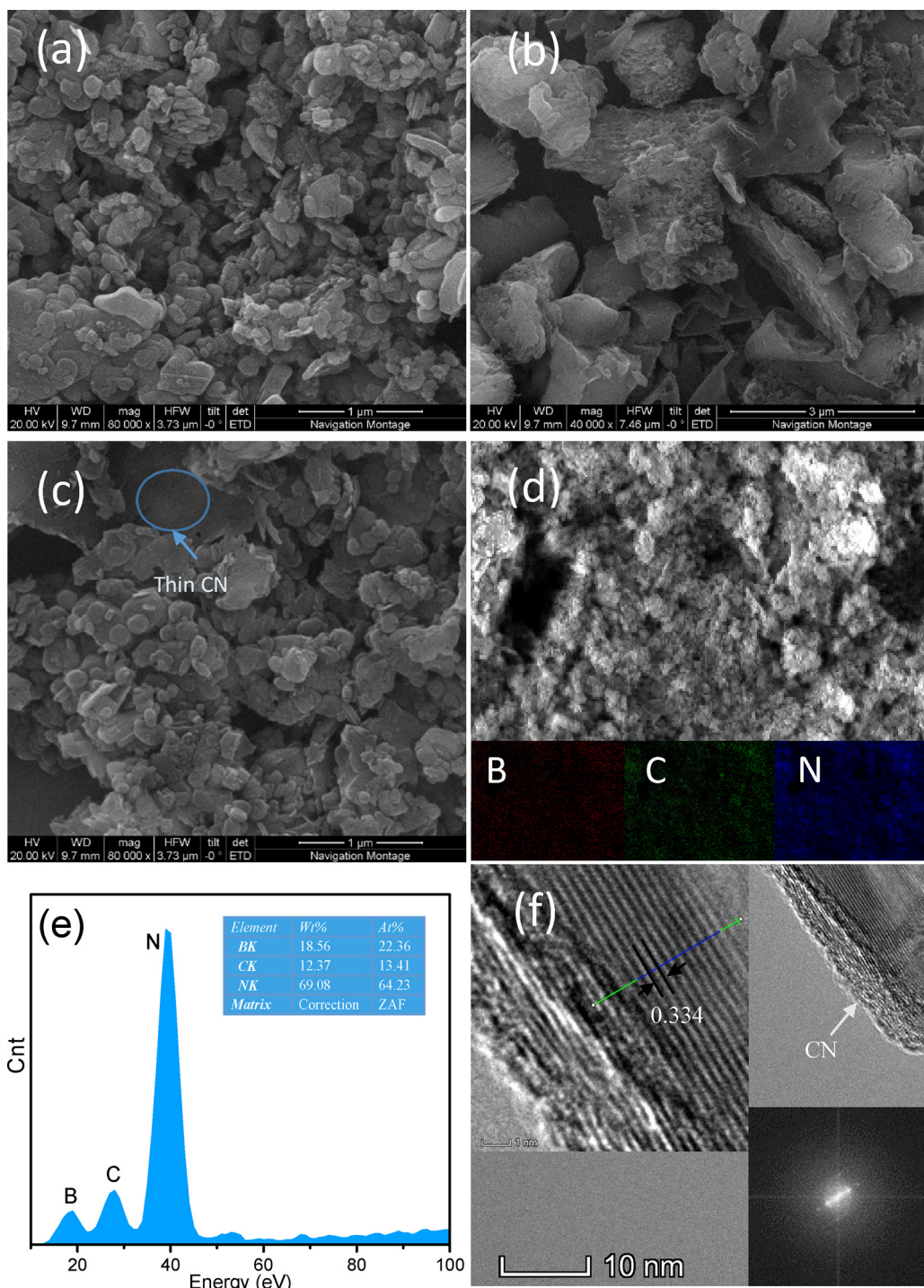


Fig. 3. SEM image of pure BN (a), CN (b) and 3-CMBN (c); (d–e) EDS mapping of 3-CMBN; (f) TEM image of 3-CMBN; and corresponding fast Fourier Transform (FFT) pattern.

granular structure of BN, where the dimensions of most nanoparticles were < 100 nm, as previously predicted, and the BN nanoparticles exhibited aggregation. It may be seen that the CN samples displayed massive, aggregated, slate-like layers in Fig. 3b [39,40]. The bulk g-C₃N₄ was the typical morphology synthesized by the facile polymerization method. The CMBN was prepared by employing BN and melamine as reactants. Different proportions of BN served as substrates to provide different surface areas for the growth of carbon nitride. The resulting polymeric graphitic carbon nitride became thinner as the quantity of BN increased. As shown in Fig. 3c, the morphology of the 3-CMBN was similar to BN, and a thin layer of CN was also generated.

Meanwhile, according to Fig. 3d and e, the content of each element could be obtained. Consequently, carbon nitride could be grown on the BN surface. Fig. 3f reveals clear lattice fringes for the identification of a crystallographic spacing of ca. 0.334 nm, which matched well with the 002 lattice planes of BN [41]. Fast Fourier Transform (FFT) analysis was obtained to reveal a displacement of ca. 0.33 nm. Since the CN wrapped on the exterior was a semi-crystalline material, it was difficult to obtain a clear lattice fringe [42].

The UV-vis diffuse reflectance spectra (DRS) of BN, CN, and a series of CMBN hybrids with different quantities of BN are depicted in Fig. 4. Pure BN revealed a restricted absorption where the visible range was

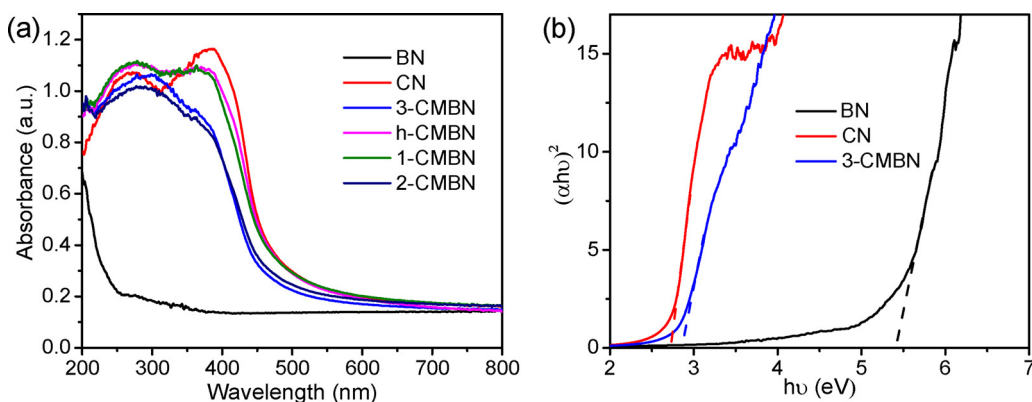


Fig. 4. (a) UV-vis diffuse reflectance spectra of BN, CN and 3-CMBN photocatalysts and (b) the corresponding Tauc plot.

not included. Pristine CN revealed a distinct absorption band at ~ 490 nm, which was consistent with the previous literature [35]. Compared with CN, 3-CMBN exhibited a slightly hypsochromic shift in the absorption edge that might have been attributed to the quantum confinement induced by the thinner CN that was generated on the surfaces of the BN nanoparticles. As shown in Fig. 4a, all the CMBN revealed remarkable visible-light absorption. Meanwhile, CMBN exhibited enhanced optical absorption at ~ 410 nm as the quantity of BN increased, which could be ascribed to the formation of new chemical species between the BN and CN.

Moreover, a greatly enhanced light-harvesting ability across the entire optical spectrum, particularly in the 530 nm–800 nm region, was also discovered for 3-CMBN, which was primarily due to the defect sites associated with the exposure of sharp edges, or the multiple reflections of incident light within hierarchical architectures [43]. However, the CN exhibited greater optical absorption in the light region between 300 nm and 465 nm than did the 3-CMBN, which indicated that the surface of the 3-CMBN was not purely thinner CN, but contained sites where chemical combinations exhibited higher activity.

To further investigate the optical properties of the CMBN, the optical bandgap could be calculated according to Eq. (1):

$$\alpha h\nu = A(h\nu - E_g)^{n/2} \quad (1)$$

Where A, E_g , α , h, and ν represent the constant, bandgap energy, the absorption coefficient, Planck constant, and light frequency, respectively. The n values of BN and CN are 1 [44,45], which are determined by the optical transition properties of a semiconductor [21,46]. As shown in Fig. 4b, the CN presented a bandgap of 2.72 eV whereas BN presented a bandgap of 5.4 eV, which were close to previously reported values [47–49]. Also, following the modification of carbon, the 3-CMBN exhibited a significantly reduced bandgap, which was estimated to be ~ 2.85 eV. This result differed from boron-doped carbon nitride [50].

Raman spectroscopy was employed to characterize the 3-CMBN and BN that were not modified by CN. Fig. 5a depicts the typical Raman spectra of the BN, where an intense peak appeared at 1367.7 cm^{-1} , which could be assigned to the E_{2g} vibration mode of BN [11,37,48]. The Raman peak of 3-CMBN at 1367.7 cm^{-1} was weakened due to the overlapping of the D peak in the top graphitic carbon nitride and the strong photoluminescence background [51]. Fig. 5b displays the FT-IR spectra of the BN, CN, and 3-CMBN. The strong FT-IR absorption peaks in the pure CN sample revealed its typical molecular structure. The serial intense bands in the 1200 – 1700 cm^{-1} region corresponded to the typical C–N and C=N stretching vibrations of the tri-s-triazine rings. The steep peak at 808 cm^{-1} represented the out-of-plane bending vibration of the tri-s-triazine units of the CN. The broad absorption band between 3000 and 3600 cm^{-1} was due to the N–H stretching vibration modes of CN [52–54]. The band observed at 806 cm^{-1} corresponded to the in-plane B–N transverse stretching vibration, whereas two bands at 1386 cm^{-1} and 1398 cm^{-1} were ascribed to the out-of-plane B–N–B

bending vibration [55]. The incorporation of carbon onto the surface of the BN led to a slight bond shift of the 3-CMBN, which may have been attributed to the distortion of the layer symmetry [11]. The C–N chemical bonds at 1635 cm^{-1} appeared clearly in the 3-CMBN, which confirmed that the melamine carbon was successfully doped with BN. The broad peak at 3422 cm^{-1} was assigned to the O–H stretching vibration from absorbed water molecules and surface resident hydroxyl groups [56,57].

To further confirm the thin layered structure on the CMBN surface, the interactions between BN and CN in the 3-CMBN were investigated using X-ray photoelectron spectroscopy (XPS). The elemental surface composition and chemical state of the 3-CMBN were analyzed by XPS. For comparison, the XPS spectra of BN and CN were also included, as shown in Fig. 6a. The survey spectra of these samples indicated that they consisted only of B, C, N, and O. A weak O1s peak at 531.0 eV could be attributed to the absorption of H_2O or CO_2 , and this phenomenon has been described in many previous papers [18]. For the BN and 3-CMBN, the B1s spectra revealed a primary binding energy of 190.7 eV (in Fig. 6b), which should be assigned to B–N [25]. Meanwhile, a 191.5 eV peak appeared, which was ascribed not to the chemical bonds of BC_xO_y or B–O, but the lower binding energy of the B–N–C moieties [58,59]. As illustrated in Fig. 6c, two peaks of the high-resolution spectra of C1s at the binding energies of 285.0 and 288.4 eV appeared in both CN and 3-CMBN, respectively. The weak shoulder peak located at 288.4 eV was assigned to N–C=N [35]. However, the 3-CMBN possessed a weaker peak intensity. Fig. 6d shows the high-resolution XPS spectra of N1s. Besides the standard sp₂-hybridized N–B peak located at the binding energy of 398.2 eV , the peaks located at 398.8 , 400.3 , 401.4 , and 404.5 eV corresponded to triazine rings (C–N=C), N–(C)₃, N–H, and graphitic species, respectively [35,60].

The formation of C–N–B bonds were further examined and confirmed. In addition, the peak with a different relative intensity located at 399.2 eV was attributed to the edge-nitrogen of BN that was linked with the melamine carbon to form the C–N–B. The doping of carbon into the BN could narrow the bandgap [48], whereas the C–N–B moieties may have been responsible for higher photocatalytic activity [58]. The above results revealed that a smaller proportion of BN provided less surface area for CN growth, resulting in the formation of a thicker CN layer. Therefore, most of the photonic energy was absorbed by the thick CN layer. When the CN layer was thinner, additional light generated energy could be utilized by the C–N–B moieties to enhance the photocatalytic activity.

3.2. Photocatalytic performance of 3-CMBN

The photocatalytic performance of the designed 3-CMBN was evaluated via the degradation of a typical personal care product (PPCP), enrofloxacin (ENFX). Here, ENFX was selected as a model organic pollutant to evaluate the photocatalytic performance of 3-CMBN

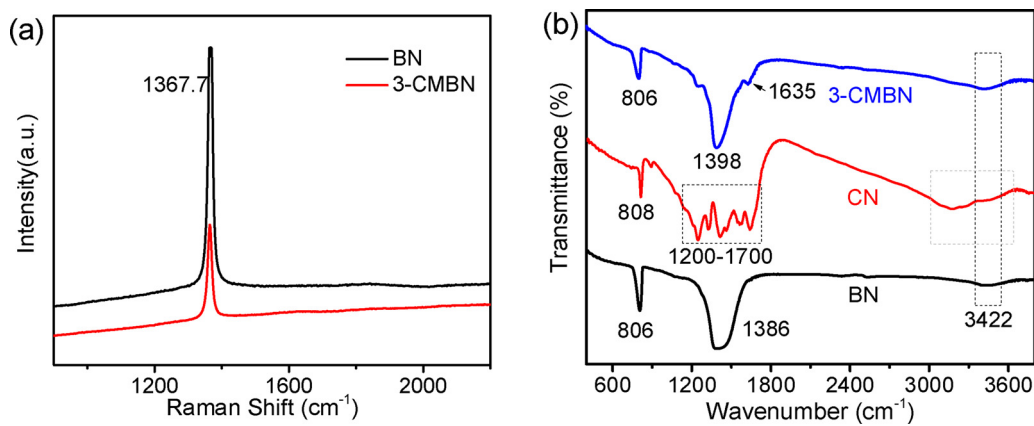


Fig. 5. (a) Raman spectra of BN and 3-CMBN; (b) FT-IR spectra of BN, CN, and 3-CMBN.

under blue-LED irradiation. ENFX cannot be decomposed in the absence of a photocatalyst, which indicated that it was resistant to photodegradation under blue-LED irradiation. Therefore, the higher specific surface area of BN was utilized to create additional photocatalytically active sites following the CN modification of BN. As Fig. 7 reveals, compared to photolysis without a photocatalyst, the introduction of BN and CN increased the degradation rate constants to 0.0024 min^{-1} and 0.038 min^{-1} , respectively. However, once the CN was modified with BN, the degradation was obviously expedited over pure BN and CN due to the formation of novel C–N–B moieties that enhanced the photocatalytic properties. The 3-CMBN appeared to be optimal for photocatalytic degradation. As shown in Fig. 7b, it was observed that the photocatalytic activity of the 3-CMBN was 39.3 and 2.4 times higher than that of pure BN and bulk CN under blue-LED irradiation,

respectively, where all the ENFX was decomposed following 60 min. of treatment. After one hour of photodegradation, the 3-CMBN mineralization rate of ENFX was 38% greater than that of CN (12%), and the photocatalytic effect of BN under blue LED illumination was negligible (Table S4). These results confirmed that CMBN played a critical role in augmenting the photocatalytic activity of BN, while revealing the novel photocatalytic effect of the CMBN. Meanwhile, it was shown that an appropriate quantity of BN, which provided the optimal specific surface area and population of surface resident active sites, markedly enhanced the photocatalytic abilities of BN. However, an excess BN failed to bind with enough CN, which resulted in a decreased degradation capacity.

As previously stated (Fig. 4), pure BN exhibited absorption in the 300 nm region, while no obvious absorption peak in the visible range was observed for BN. The absorption intensity of BN was broadened

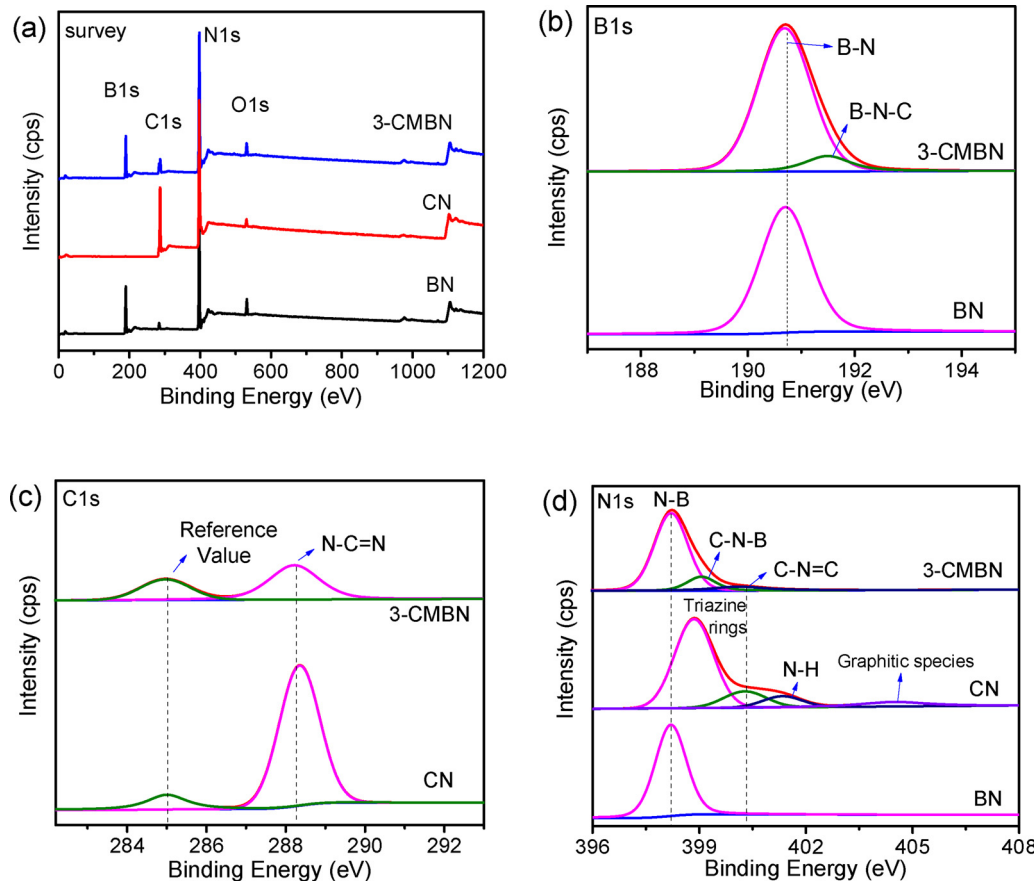


Fig. 6. XPS analysis of BN, CN and 3-CMBN: (a) the full-scale XPS spectrum; high resolution XPS spectra of B1s (b), C1s (c), and N1s (d).

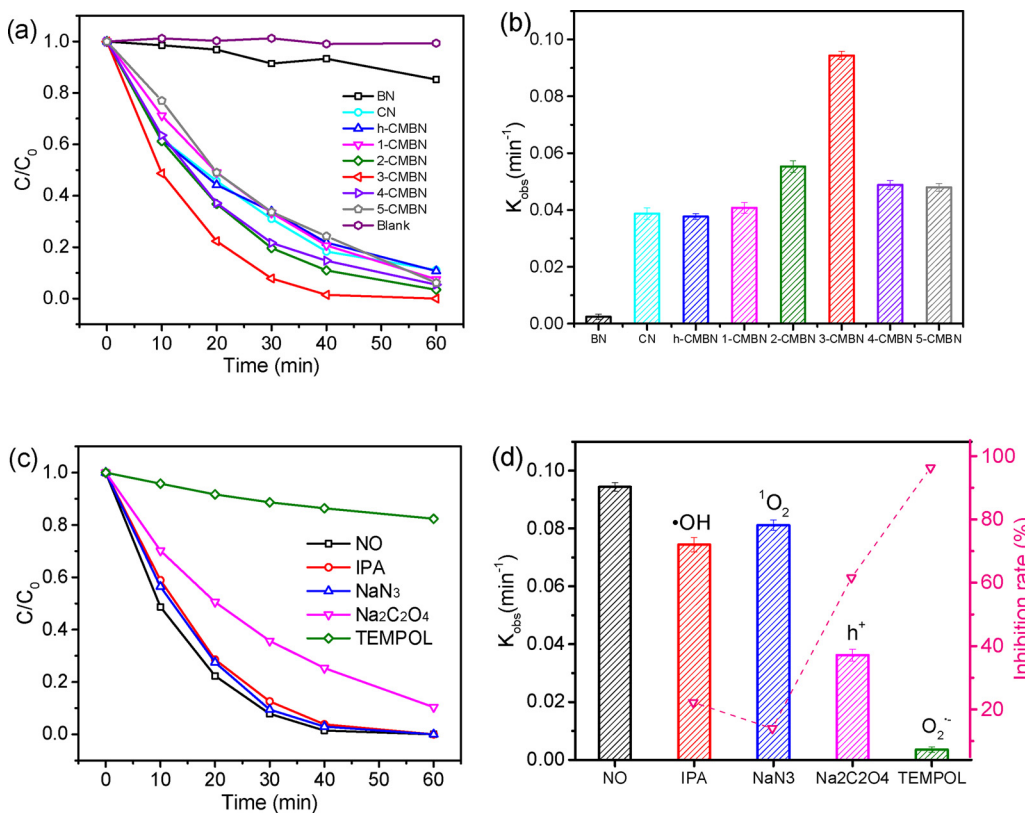


Fig. 7. (a) Photocatalytic degradation of ENFX with different photocatalysts under blue LED light irradiation; (b) Kinetic rate constant of ENFX degradation over different photocatalysts; (c) Photocatalytic degradation of ENFX under blue LED light irradiation with addition of different scavengers using 3-CMBN photocatalyst. (d) Kinetic rate constant of ENFX (bar, left y-axis) and the inhibition rate of RSs (pink curve, right y-axis).

with the modification of melamine carbon, where BN was doped with melamine as a carbon source to form the C–N–B species. This might be regarded as a conclusive basis for the enhancement of photocatalytic activity under blue-LED illumination. Higher BN content within the composites provided a more extensive surface to facilitate doping. Quantitative melamine may have been more evenly distributed on the BN surface such that the melamine carbon was attached to BN and less polymerization occurred to form CN. However, excess BN led to an obvious decrease in photocatalytic activity (Fig. 7). Although a higher BN content within the composites provided an excessive surface for doping, only a certain amount of CN modified the surfaces of a limited number of BN. Therefore, not all the blue light could access the more highly photocatalytically active C–N–B bond sites. Hence, only a certain percentage of the light that illuminated the surface of the pure BN was absorbed for improved photodegradation. In summary, it was obvious that the modification of CN to BN could enhance the visible blue light photocatalytic activity of the composites.

3.3. Roles of reactive species (RSs)

Various reactive species (e.g., O₂^{·-}, OH, ¹O₂, h⁺) played different roles in the photocatalytic degradation of ENFX. A number of scavengers were employed in this study to further identify their respective roles toward the photocatalytic degradation of ENFX. Typically, 10 mM isopropanol (IPA) served as the hydroxyl radical (OH) scavenger, 75 mM sodium azide (Na₃) was the singlet oxygen (¹O₂) scavenger, 10 mM sodium oxalate (Na₂C₂O₄) was the photogenerated hole (h⁺) scavenger, and 1.0 mM 4-hydroxy-2,2,6,6-tetramethylpiperidinyloxy (TEMPOL) was the superoxide iron radical (O₂^{·-}) scavenger [26,61–63]. As illustrated in Fig. 7c and d, a more rapid reaction rate was observed without the addition of scavengers, with a photocatalytic degradation rate constant of 0.0944 min⁻¹, whereas Na₃ and IPA showed a slight inhibitory effect on the degradation of ENFX, with rate constants of 0.081 min⁻¹ and 0.074 min⁻¹, respectively. These results indicated that OH and ¹O₂ had negligible effects, which meant that the

inhibiting effects of Na₃ and IPA were 14.0% and 21.2%, respectively. However, the addition of Na₂C₂O₄ produced a greater inhibitory effect than Na₃ and IPA, with a rate constant of 0.0362 min⁻¹. This phenomenon revealed that h⁺ played a more important role than did OH and ¹O₂ during the photodegradation of ENFX. What is more, following the addition of TEMPOL, a remarkably restrictive effect was observed with a rate constant of 0.0035 min⁻¹ for the photocatalytic process, which signified an inhibition level of 96.3%. These results confirmed that O₂^{·-} and h⁺ played critical roles in the photocatalytic degradation of ENFX.

To investigate the generation of radicals during the in-depth reaction process, the spin-trapping EPR signals of BN, CN, and 3-CMBN were obtained with DMPO in a methanol dispersion of DMPO-O₂^{·-}, as well as an aqueous dispersion of DMPO-OH [64–66]. These experiments were conducted under dark conditions and visible light irradiation of 5 min. and 10 min. As shown in Fig. 8a, no O₂^{·-} radical signals were detected for BN, CN, and 3-CMBN while the system remained in the dark, and no signals for O₂^{·-} radicals were observed for BN under visible light irradiation. According to the UV-vis DRS characterization, the failure to detect O₂^{·-} radicals in pure BN was ascribed to the wide bandgap. Hence, it was difficult to excite BN under visible light to generate electron-hole pairs, and to further produce O₂^{·-} radicals. It can be seen from Fig. 8a that EPR signals could be detected for CN under illuminated conditions, while four-line EPR signals with intensity ratios of 1:1:1:1 were observed under visible light conditions. Meanwhile, the EPR signals for the 3-CMBN were more significant than CN, which might have been ascribed to the lower recombination of photo-generated electron-hole pairs. As depicted in Fig. 8b, negligible EPR signals for OH radicals were observed for CN and 3-CMBN under dark conditions, whereas no EPR signals were directly detected for BN under both dark and light conditions. The photogenerated holes of pure BN had a higher oxidation power than did OH radicals, which was (in theory) due to the valence-band maximum of BN being more positive. However, no BN signals were detected that could be ascribed to the bandgap being too wide to be excited. These obvious EPR signals for

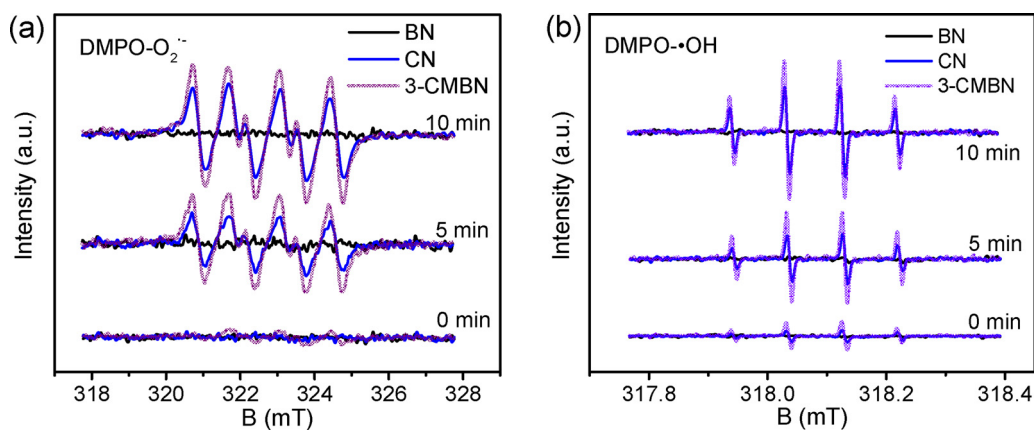


Fig. 8. EPR spectra of the (a) DMPO-O₂[•]- and (b) DMPO-OH adducts recorded with BN, CN and 3-CMBN under blue LED light irradiation.

OH radicals were obtained for CN and 3-CMBN under visible light illumination, while four-line EPR signals with intensity ratios of 1:2:2:1 were observed. These four-line EPR signals were similar to those described by Wang. et al. [23,67]. However, the O₂[•]- radical signal was greatly enhanced for the 3-CMBN sample, whereas the OH radical signal was also simultaneously improved (Fig. 8a and b). These results verified the increased photocatalytic activity of CN-modified BN as being consistent with the results of the photocatalytic degradation of ENFX [68,69].

To investigate the stability of the 3-CMBN photocatalysts, recycling experiments were conducted under identical conditions. As Fig. 9a shows, the photocatalytic degradation rate of ENFX was obviously not decreased following four recycling runs. Further, the characteristic stretching was not obviously altered, as shown in Fig. 9b. These results revealed that the 3-CMBN exhibited outstanding structural stability.

3.4. Product identification and theoretical calculations

HPLC-Q-TOF, GC-MS, and IC were employed to identify the intermediates formed during the photocatalytic degradation of ENFX. Table S1 provides detailed information on the fourteen intermediate products that were identified by HPLC-Q-TOF, and GC-MS, which also detected two intermediate products (Table S2).

Furthermore, theoretical calculations were utilized to predict which sites were preferentially attacked by the reactive species. The frontier electron densities (FEDs) data of the ENFX molecules were calculated to speculate on the reaction process, as summarized in Fig. S3 and Table S3. The C1, C2, C5, C10, N18, and N28 positions exhibited higher FED_{HOMO}² + FED_{LUMO}² values, which indicated that these sites were

more likely to undergo OH attacks in an electrophilic reaction. The C4, C6, C8, C10, and C13 positions of ENFX revealed more positive point charges than others, which translated to these sites being more vulnerable to attack by O₂[•]- radicals for nucleophilic addition reactions [70]. Typical ion spectra showed a *m/z* of 360.2, which was detected at RT = 8.7 min. in the original ENFX solution. This *m/z* was consistent with the molecular mass of ENFX in a positive ion model.

According to intermediate degradation product identification and reactive site prediction, potential photocatalytic degradation pathways of ENFX over the 3-CMBN photocatalysts under blue LED light were proposed, including hydroxylation, oxidation, reduction reaction, dealkylation, and dehydration. The potential photocatalytic degradation pathways of ENFX are proposed in Scheme 1. Three potential pathways were proposed as follows: Pathway I was primarily a nucleophilic addition reaction. Carbonyl is a polar group, and the carbon atom (C8) possessed a partially positive charge, which corresponded to theoretical calculations, and led to the initial formation of E1. Subsequently, C8, C10, and N18 were attacked by the strong oxidizing capacity of the reactive groups (O₂[•]- or/and h⁺), and the ·OH radicals generated the E2-E4 products [71]. Pathway II primarily involved the interactions of various active species. N28 was attacked by ·OH radicals and other oxidizing groups, and the fluorine atom in ENFX was displaced with a hydroxyl group to form E5, E6, E7, E8, and E9. E9 was further transformed E10 via oxidation. Pathway III primarily included different positions that were substituted with one or two hydroxyl groups to form E11, E12, and E13. A similar pathway was present during the photocatalytic degradation of CIP [72]. As the E11 and E13 structures were unstable, the quinolone ring was broken, which formed E14. Additionally, these intermediate products might undergo a series

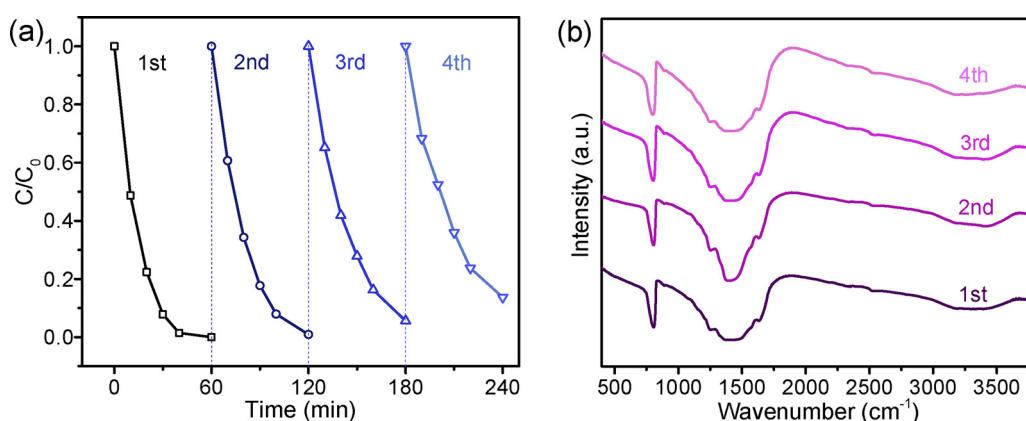
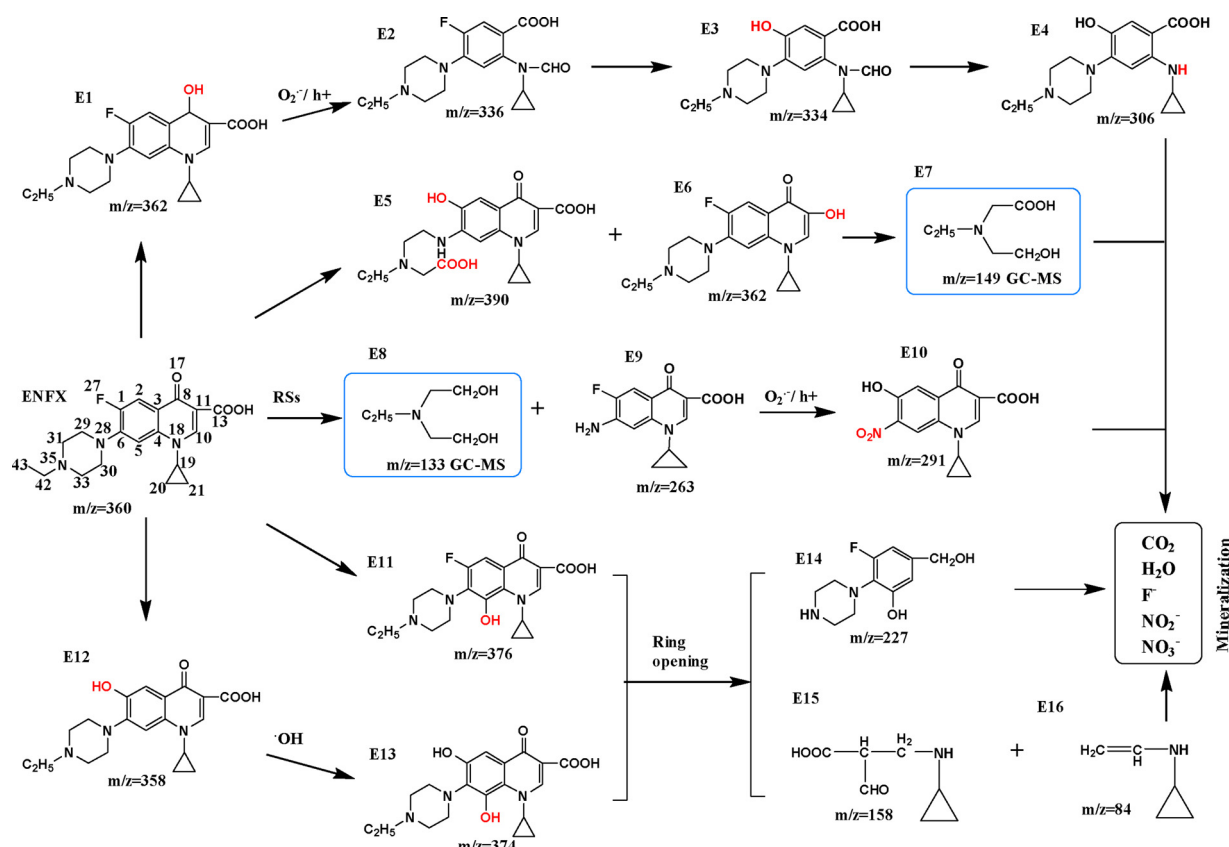
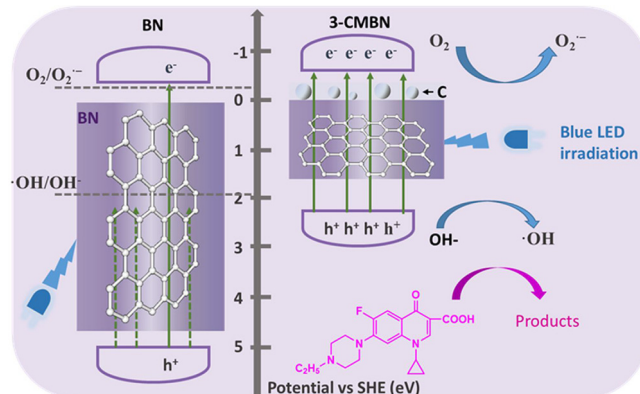


Fig. 9. (a)Photocatalytic degradation activity after four cycles of 3-CMBN photocatayst under blue LED light irradiation; (b) the FT-IR spectrum of 3-CMBN before and in each of the three replicates.



Scheme 1. Potential photocatalytic degradation pathways of ENFX in 3-CMBN aqueous solution under blue LED light irradiation.



Scheme 2. Proposed photocatalytic degradation mechanisms in the 3-CMBN under blue LED light irradiation.

of reactions as the quinolone is destroyed, or additional oxidation occurs to form E15 and E16. Ultimately, a portion of the intermediate products could also undergo the cleavage of piperazine rings and decarboxylation, which were eventually mineralized to CO_2 , H_2O , NO_3^- , NO_2^- and F^- [71,73].

3.5. Mechanism of the improved photocatalytic activity of CMBN

The enhanced photocatalytic activity of CMBN in the degradation of enrofloxacin (ENFX) initially benefitted from the high specific surface area of BN. It was essential that the CN nanoparticles were evenly distributed on the BN surfaces, which prevented the aggregation of CN nanoparticles during the recycling process. This also facilitated the adhesion of adsorbents, which prompted the photocatalysis reaction, while maintaining optimal cyclability [18,74]. Melamine carbon was

homogeneously anchored to BN, whereas the adsorption of ENFX on BN increased the degradation of the organic pollutant on the loaded carbon, thus increasing the photoreaction rates. As stated above, the absorbed ENFX was gradually degraded, which left vacancies for further ENFX absorption during the photocatalytic process, thus maintaining adsorption equilibrium and promoting ENFX degradation. An additional significant contributing factor was the formation of new active chemical bonding species (C–N–B), which led to the narrowed bandgap of 3-CMBN over BN. This acted to induce excited wavelength broadening from the UV light region to the visible light range.

Further, the C–N–B bonds enabled favorable conditions for photogenerated hole-electron pairs, which created suitable new photocatalysts with an appropriate bandgap. Carbon-free BN, synthesized as such, was a typical insulator with a bandgap of ~5.4 eV. As shown in Fig. 5, the optical absorption edge of the 3-CMBN was red-shifted as the result of modification by C, which was derived from melamine. From Fig. S4, the energy bands of the BN and 3-CMBN structures were determined via Mott-Schottky plots. These positively sloped curves represented the typical n-type semiconductor properties of the as-prepared samples. Subsequently, the valence band (VB) potentials of BN and 3-CMBN were calculated as + 5.01 eV and + 2.25 eV, respectively. As Scheme 2 reveals, since the conduction band potential of 3-CMBN was more negative than the standard redox potential $\text{O}_2/\text{O}_2^\cdot^-$ (-0.33 eV) the photogenerated electrons could react with oxygen to generate O_2^\cdot [75]. Additionally, the valence band of the 3-CMBN was more positive than the standard redox potential OH/OH^- (+1.99 eV). However, it was below the potential of $\text{OH}/\text{H}_2\text{O}$ (+2.73 eV) [26], thus h^+ could oxidize OH^- to give $\cdot\text{OH}$, whereas the amount was negligible in line with the quenching experiment.

Photocurrent spectroscopy was applied to detect transient photocurrent responses and to validate the electron-hole transfer mechanism (Fig. 10a). A higher transient photocurrent response was obtained from the 3-CMBN in contrast to BN and CN, which demonstrated the more

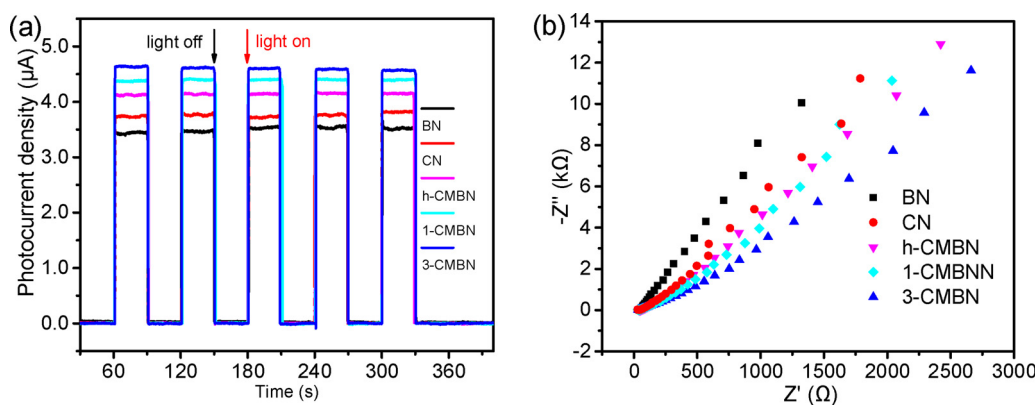


Fig. 10. (a) Transient photocurrent density responses of BN, CN, h-CMBN, 1-CMBN and 3-CMBN sample electrodes with light on/off cycles under blue LED light irradiation; (b) electrochemical impedance spectroscopy (EIS) plots of the BN, CN, h-CMBN, 1-CMBN and 3-CMBN.

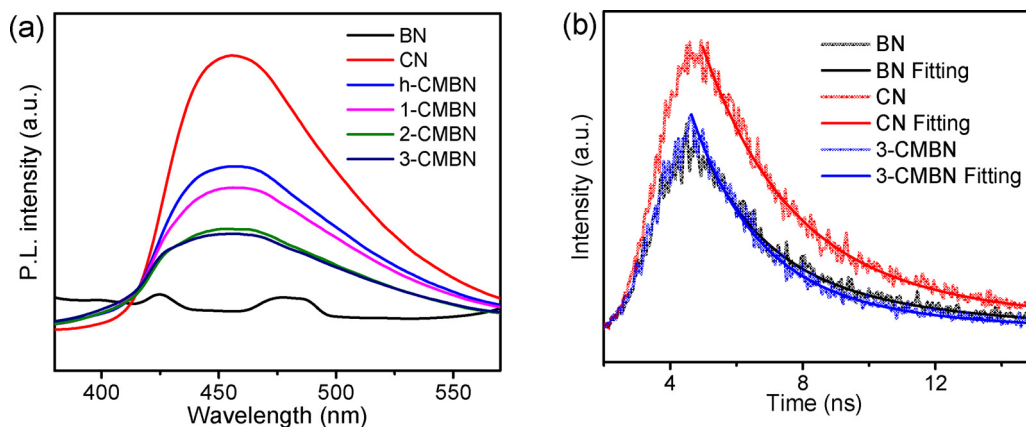


Fig. 11. Photoluminescence spectra (a), and fluorescence decay (b) of BN, CN and 3-CMBN excitation at 300 nm.

efficient separation of photogenerated electron-holes [26]. Charge separation efficiencies could also be investigated through EIS (Fig. 10b). The smaller arc radius of the 3-CMBN implied a higher charge transfer efficiency. The PL analysis of BN, CN, and 3-CMBN is depicted in Fig. 11a. These samples were activated under an excitation wavelength of 300 nm. The BN exhibited an insignificant emission peak, likely due to its wide bandgap, which could not be excited. The PL intensity of the 3-CMBN decreased remarkably in contrast to CN, which revealed that the modification of carbon efficiently enhanced the separation of photo-excited charges and holes [21]. Therefore, it could be concluded that the modification of carbon might promote the migration and separation efficacy of photogenerated carriers. Meanwhile, to probe the specific charge carrier dynamics of the BN, CN, and 3-CMBN, time-resolved photoluminescence spectra were recorded and demonstrated in Fig. 11b.

It was clear that the average emission lifetime of the 3-CMBN (4.2 ns) was shorter than that of CN (4.5 ns) and BN (6.5 ns). This result differed from ultrathin graphitic carbon nitride [76], and the decreased carrier lifetime showed significantly accelerated photo-exciton dissociation in the 3-CMBN sample via a non-radiative quenching pathway [77–80]. Thus, the improvement of the photocatalytic performance was neither simply due to the formation of ultrathin carbon nitride, nor to the boron-doped carbon nitride, but rather that the CN-modified BN enabled the formation of C–N–B species.

4. Conclusion

In summary, we demonstrated that CMBN with a new active chemical bonding species (C–B–N) was successfully synthesized using a facile hydrothermal-calcination method. Through modification with

melamine carbon, this novel CMBN species, in contrast to BN, was endowed with the capacity to be responsive to visible light, and demonstrated excellent photocatalytic properties for the degradation of ENFX under blue LED light. As expected, the modified material, particularly 3-CMBN, revealed an apparent rate constant k , which was ~39.3 times higher than that of carbon-free BN for ENFX abatement. This work resulted in the development of novel multifunctional CMBN photocatalysts that can be activated by affordable blue LED light, and provides a new orientation to guide the further development of advanced photocatalysts with excellent visible light-driven characteristics.

Acknowledgements

This work was supported by the National Natural Science Foundation of China (No. 21377031 and 21677040), Science and Technology Planning Project of Guangdong Province (No. 2017A050506052).

Appendix A. Supplementary data

Supplementary material related to this article can be found, in the online version, at doi:<https://doi.org/10.1016/j.apcatb.2018.07.053>.

References

- [1] Y. Zhang, Y.W. Tan, H.L. Stormer, P. Kim, Experimental observation of the quantum Hall effect and Berry's phase in graphene, *Nature* 438 (2005) 201–204.
- [2] C. Lee, X. Wei, J.W. Kysar, J. Hone, Measurement of the elastic properties and intrinsic strength of monolayer graphene, *Science* 321 (2008) 385–388.
- [3] X. She, J. Wu, J. Zhong, H. Xu, Y. Yang, R. Vajtai, J. Lou, Y. Liu, D. Du, H. Li,

- Oxygenated monolayer carbon nitride for excellent photocatalytic hydrogen evolution and external quantum efficiency, *Nano Energy* 27 (2016) 138–146.
- [4] Q. Li, X. Li, S. Wageh, A.A. Al-Ghamdi, J. Yu, CdS/graphene nanocomposite photocatalysts, *Adv. Energy Mater.* 5 (2015).
- [5] Q. Weng, X. Wang, X. Wang, Y. Bando, D. Golberg, Functionalized hexagonal boron nitride nanomaterials: emerging properties and applications, *Chem. Soc. Rev.* 45 (2016) 3989–4012.
- [6] X.F. Jiang, Q. Weng, X.B. Wang, X. Li, J. Zhang, D. Golberg, Y. Bando, Recent progress on fabrications and applications of boron nitride nanomaterials: a review, *J. Mater. Sci. Technol.* 31 (2015) 589–598.
- [7] R.T. Paine, C.K. Narula, Synthetic routes to boron nitride, *Chem. Rev.* 90 (1990) 73–91.
- [8] W. Lei, D. Portehault, D. Liu, S. Qin, Y. Chen, Porous boron nitride nanosheets for effective water cleaning, *Nat. Commun.* 4 (2016) 1777.
- [9] M. López-Suárez, G. Abadal, L. Gammaitoni, R. Rurali, Noise energy harvesting in buckled BN nanoribbons from molecular dynamics, *Nano Energy* 15 (2015) 329–334.
- [10] Z. He, C. Kim, L. Lin, T.H. Jeon, S. Lin, X. Wang, W. Choi, Formation of heterostructures via direct growth CN on h-BN porous nanosheets for metal-free photocatalysis, *Nano Energy* (2017) 42.
- [11] J. Yu, L. Qin, Y. Hao, S. Kuang, X. Bai, Y.M. Chong, W. Zhang, E. Wang, Vertically aligned boron nitride nanosheets: chemical vapor synthesis, ultraviolet light emission, and superhydrophobicity, *ACS Nano* 4 (2010) 414–422.
- [12] Q. Weng, Y. Ide, X. Wang, X. Wang, C. Zhang, X. Jiang, Y. Xue, P. Dai, K. Komaguchi, Y. Bando, Design of BN porous sheets with richly exposed (002) plane edges and their application as TiO₂ visible light sensitizer, *Nano Energy* 16 (2015) 19–27.
- [13] M. Wang, M. Li, L. Xu, L. Wang, Z. Ju, G. Li, Y. Qian, High yield synthesis of novel boron nitride submicro-boxes and their photocatalytic application under visible light irradiation, *Catal. Sci. Technol.* 1 (2011) 1159–1165.
- [14] X. Fu, Y. Hu, T. Zhang, S. Chen, The role of ball milled h-BN in the enhanced photocatalytic activity: a study based on the model of ZnO, *Appl. Surf. Sci.* 280 (2013) 828–835.
- [15] Y. Song, H. Xu, C. Wang, J. Chen, J. Yan, Y. Xu, Y. Li, C. Liu, H. Li, Y. Lei, Graphene-analogue boron nitride/Ag₃Po₄ composite for efficient visible-light-driven photocatalysis, *RSC Adv.* 4 (2014) 56853–56862.
- [16] J. Chen, J. Zhu, Z. Da, H. Xu, J. Yan, H. Ji, H. Shu, H. Li, Improving the photocatalytic activity and stability of graphene-like BN/AgBr composites, *Appl. Surf. Sci.* 313 (2014) 1–9.
- [17] H. Xu, L. Liu, Y. Song, L. Huang, Y. Li, Z. Chen, Q. Zhang, H. Li, BN nanosheets modified WO₃ photocatalysts for enhancing photocatalytic properties under visible light irradiation, *J. Alloys Compd.* 660 (2016) 48–54.
- [18] S. Meng, X. Ye, X. Ning, M. Xie, X. Fu, S. Chen, Selective oxidation of aromatic alcohols to aromatic aldehydes by BN/metal sulfide with enhanced photocatalytic activity, *Appl. Catal. B* 182 (2016) 356–368.
- [19] J. Di, J. Xia, M. Ji, B. Wang, Y. Sheng, Z. Qi, Z. Chen, H. Li, Advanced photocatalytic performance of graphene-like BN modified BiOBr flower-like materials for the removal of pollutants and mechanism insight, *Appl. Catal. B* 183 (2016) 254–262.
- [20] J. Zhang, M. Zhang, R.Q. Sun, X. Wang, A facile band alignment of polymeric carbon nitride semiconductors to construct isotype heterojunctions, *Angew. Chem. Int. Ed.* 51 (2012) 10145.
- [21] Z. Xie, Y. Feng, F. Wang, D. Chen, Q. Zhang, Y. Zeng, W. Lv, G. Liu, Construction of carbon dots modified MoO₃/g-C₃N₄ Z-scheme photocatalyst with enhanced visible-light photocatalytic activity for the degradation of tetracycline, *Appl. Catal., B* 229 (2018) 96–104.
- [22] L. Jiang, X. Yuan, G. Zeng, X. Chen, Z. Wu, J. Liang, J. Zhang, H. Wang, H. Wang, Phosphorus- and sulfur-codoped g-C₃N₄: facile preparation, mechanism insight, and application as efficient photocatalyst for tetracycline and methyl orange degradation under visible light irradiation, *ACS Sustain. Chem. Eng.* 5 (2017) 5831–5841.
- [23] P. Chen, F. Wang, Q. Zhang, Y. Su, L. Shen, K. Yao, Z.F. Chen, Y. Liu, Z. Cai, W. Lv, Photocatalytic degradation of clofibrate acid by g-C₃N₄/P25 composites under simulated sunlight irradiation: the significant effects of reactive species, *Chemosphere* 172 (2017) 193.
- [24] L. Jiang, X. Yuan, G. Zeng, J. Liang, Z. Wu, H. Wang, Construction of all-solid-state Z-scheme photocatalyst based on graphite carbon nitride and its enhancement to catalytic activity, *Environ. Sci. Nano* (2018).
- [25] L. Jiang, X. Yuan, G. Zeng, Z. Wu, J. Liang, X. Chen, L. Leng, H. Wang, H. Wang, Metal-free efficient photocatalyst for stable visible-light photocatalytic degradation of refractory pollutant, *Appl. Catal. B* (2017) 221.
- [26] Q. Zhang, P. Chen, M. Zhuo, F. Wang, Y. Su, T. Chen, K. Yao, Z. Cai, W. Lv, G. Liu, Degradation of indometacin by simulated sunlight activated CDs-loaded BiPO₄ photocatalyst: roles of oxidative species, *Appl. Catal. B* 221 (2018) 129–139.
- [27] Y. Su, P. Chen, F. Wang, Q. Zhang, T. Chen, Y. Wang, K. Yao, W. Lv, G. Liu, Decoration of TiO₂/g-C₃N₄ Z-scheme by carbon dots as a novel photocatalyst with improved visible-light photocatalytic performance for the degradation of enrofloxacin, *RSC Adv.* 7 (2017) 34096–34103.
- [28] D. Barceló, M. Petrović, Pharmaceuticals and personal care products (PPCPs) in the environment, *Anal. Bioanal. Chem.* 387 (2007) 1141–1142.
- [29] A. Jia, Y. Wan, Y. Xiao, J. Hu, Occurrence and fate of quinolone and fluorquinolone antibiotics in a municipal sewage treatment plant, *Water Res.* 46 (2012) 387–394.
- [30] T.S. Anirudhan, F. Shainy, J. Christa, Synthesis and characterization of polyacrylic acid- grafted-carboxylic graphene/titanium nanotube composite for the effective removal of enrofloxacin from aqueous solutions: adsorption and photocatalytic degradation studies, *J. Hazard. Mater.* 324 (2016) 117–130.
- [31] C. Zheng, G. He, X. Xiao, M. Lu, H. Zhong, X. Zuo, J. Nan, Selective photocatalytic oxidation of benzyl alcohol into benzaldehyde with high selectivity and conversion ratio over Bi 4 O 5 Br 2 nanoflakes under blue LED irradiation, *Appl. Catal. B* (2016) 205.
- [32] J.P. Ghosh, C.H. Langford, G. Achari, Characterization of an LED based photoreactor to degrade 4-chlorophenol in an aqueous medium using coumarin (C-343) sensitized TiO₂, *J. Phys. Chem. A* 112 (2008) 10310.
- [33] X. Wang, T.T. Lim, Solvothermal synthesis of C-N codoped TiO₂ and photocatalytic evaluation for bisphenol A degradation using a visible-light irradiated LED photoreactor, *Appl. Catal. B* 100 (2010) 355–364.
- [34] S. Abele, F.Q. Nie, F. Foret, B. Paull, M. Macka, UV-LED photopolymerised monoliths, *Analyst* 133 (2008) 864–866.
- [35] F. Wang, P. Chen, Y. Feng, Z. Xie, Y. Liu, Y. Su, Q. Zhang, Y. Wang, K. Yao, W. Lv, Facile synthesis of N-doped carbon dots/g-C₃N₄ photocatalyst with enhanced visible-light photocatalytic activity for the degradation of indomethacin, *Appl. Catal. B* 207 (2017) 103–113.
- [36] J. Liu, T. Zhang, Z. Wang, G. Dawson, W. Chen, Simple pyrolysis of urea into graphitic carbon nitride with recyclable adsorption and photocatalytic activity, *J. Mater. Chem. B* (2011) 14398–14401.
- [37] Y. Shi, C. Hamson, X. Jia, K.K. Kim, A. Reina, M. Hofmann, A.L. Hsu, K. Zhang, H. Li, Z.Y. Juang, Synthesis of few-layer hexagonal boron nitride thin film by chemical vapor deposition, *Nano Lett.* 10 (2010) 4134.
- [38] W. Zhu, X. Gao, Q. Li, H. Li, Y. Chao, M. Li, S.M. Mahurin, H. Li, H. Zhu, S. Dai, Controlled gas exfoliation of boron nitride into few-layered nanosheets, *Angew. Chem. Int. Ed.* 55 (2016) 10766–10770.
- [39] W. Wu, W. Xu, X. An, L. Wang, J. Zhang, Z. Li, M. Wu, Multiaspect insight into synergistic modification of carbon nitride with halide salt and water vapor, *Appl. Catal. B* (2018) 229.
- [40] Z. Zeng, H. Yu, X. Quan, S. Chen, S. Zhang, Structuring phase junction between tri-s-triazine and triazine crystalline G₃N₄ for efficient photocatalytic hydrogen evolution, *Appl. Catal. B* (2018).
- [41] D. Liu, W. Lei, S. Qin, Y. Chen, Template-free synthesis of functional 3D BN architecture for removal of dyes from water, *Sci. Rep.* 4 (2014) 4453.
- [42] M. Fu, J. Liao, F. Dong, H. Li, H. Liu, Growth of g-C₃N₄ layer on commercial TiO₂ for enhanced visible light photocatalytic activity, *J. Nanomater.* 2014 (2014) 1–8.
- [43] J. Zhang, M. Zhang, C. Yang, X. Wang, Nanospherical carbon nitride frameworks with sharp edges accelerating charge collection and separation at a soft photocatalytic interface, *Adv. Mater.* 26 (2014) 4121–4126.
- [44] J. Liu, Y. Liu, N. Liu, Y. Han, X. Zhang, H. Huang, Y. Lifshitz, S.T. Lee, J. Zhong, Z. Kang, Metal-free efficient photocatalyst for stable visible water splitting via a two-electron pathway, *Science* 347 (2015) 970–974.
- [45] R. Sevak Singh, R. Yingjie Tay, W. Leong Chow, S. Hon Tsang, G. Mallick, E.H.T. Teo, Band gap effects of hexagonal boron nitride using oxygen plasma, *Appl. Phys. Lett.* 104 (2014) 932.
- [46] Y. Xia, Q. Li, K. Lv, D. Tang, M. Li, Superiority of graphene over carbon analogs for enhanced photocatalytic H₂-production activity of ZnIn₂S₄, *Appl. Catal. B* 206 (2017) 344–352.
- [47] C. Tang, Y. Bando, Y. Huang, S. Yue, C. Gu, F. Xu, D. Golberg, Fluorination and electrical conductivity of BN nanotubes, *J. Am. Chem. Soc.* 127 (2005) 6552–6553.
- [48] C. Huang, C. Chen, M. Zhang, L. Lin, X. Ye, S. Lin, M. Antonietti, X. Wang, Carbon-doped BN nanosheets for metal-free photoredox catalysis, *Nat. Commun.* 6 (2015) 7698.
- [49] L. Jiang, X. Yuan, Y. Pan, J. Liang, G. Zeng, Z. Wu, H. Wang, Doping of graphitic carbon nitride for photocatalysis: a review, *Appl. Catal., B* 217 (2017) 388–406.
- [50] Z. Lin, X. Wang, Nanostructure engineering and doping of conjugated carbon nitride semiconductors for hydrogen photosynthesis, *Angew. Chem. Int. Ed. Engl.* 52 (2013) 1735–1738.
- [51] C. Zhang, S. Zhao, C. Jin, A.L. Koh, Y. Zhou, W. Xu, Q. Li, Q. Xiong, H. Peng, Z. Liu, Direct growth of large-area graphene and boron nitride heterostructures by a co-segregation method, *Nat. Commun.* 6 (2015) 6519.
- [52] Y. Tan, Z. Shu, J. Zhou, T. Li, W. Wang, Z. Zhao, One-step synthesis of nanostructured g-C₃N₄/TiO₂ composite for highly enhanced visible-light photocatalytic H₂ evolution, *Appl. Catal., B* 230 (2018) 260–268.
- [53] R. Wang, X. Kong, W. Zhang, W. Zhu, L. Huang, J. Wang, X. Zhang, X. Liu, N. Hu, Y. Suo, Mechanism insight into rapid photocatalytic disinfection of salmonella based on vanadate QDs-interspersed g-C₃N₄ heterostructures, *Appl. Catal. B* (2017).
- [54] L. Ye, J. Liu, Z. Jiang, T. Peng, L. Zan, Facets coupling of BiOBr-g-C₃N₄ composite photocatalyst for enhanced visible-light-driven photocatalytic activity, *Appl. Catal. B* 142–143 (2013) 1–7.
- [55] W. Gao, L.B. Alemany, L. Ci, P.M. Ajayan, New insights into the structure and reduction of graphite oxide, *Nat. Chem.* 1 (2009) 403–408.
- [56] J. Qu, Y. Wang, J. Guo, Y. Dong, T. Lou, Sensitive simultaneous determination of hydroquinone and catechol based on BCN graphene and poly(alizarin red S), *J. Electrochem. Soc.* 161 (2014) B220–B224.
- [57] I. Kaminska, M.R. Das, Y. Coffinier, J. Niedziolkajonsson, J. Sobczak, P. Woisel, J. Lyskawa, M. Opallo, R. Boukherroub, S. Szunerits, Reduction and functionalization of graphene oxide sheets using biomimetic dopamine derivatives in one step, *ACS Appl. Mater. Interfaces* 4 (2012) 1016.
- [58] J.I. Ozaki, N. Kimura, T. Anahara, A. Oya, Preparation and oxygen reduction activity of BN-doped carbons, *Carbon* 45 (2007) 1847–1853.
- [59] J.I. Ozaki, T. Anahara, N. Kimura, A. Oya, Simultaneous doping of boron and nitrogen into a carbon to enhance its oxygen reduction activity in proton exchange membrane fuel cells, *Carbon* 44 (2006) 3358–3361.
- [60] F. Wang, Y. Wang, Y. Feng, Y. Zeng, Z. Xie, Q. Zhang, Y. Su, P. Chen, Y. Liu, K. Yao, Novel ternary photocatalyst of single atom-dispersed silver and carbon quantum dots co-loaded with ultrathin g-C₃N₄ for broad spectrum photocatalytic

- degradation of naproxen, *Appl. Catal. B* (2017) 221.
- [61] F. Chen, Q. Yang, X. Li, G. Zeng, D. Wang, C. Niu, J. Zhao, H. An, T. Xie, Y. Deng, Hierarchical assembly of graphene-bridged Ag 3 PO 4 /Ag/BiVO 4 (040) Z-scheme photocatalyst: an efficient, sustainable and heterogeneous catalyst with enhanced visible-light photoactivity towards tetracycline degradation under visible light irradiation, *Appl. Catal. B* 200 (2017) 330–342.
- [62] F. Chen, Q. Yang, S. Wang, F. Yao, J. Sun, Y. Wang, C. Zhang, X. Li, C. Niu, D. Wang, Graphene oxide and carbon nitride nanosheets co-modified silver chromate nanoparticles with enhanced visible-light photoactivity and anti-photo-corrosion properties towards multiple refractory pollutants degradation, *Appl. Catal. B* 209 (2017) 493–505.
- [63] L. Jiang, X. Yuan, G. Zeng, J. Liang, X. Chen, H. Yu, H. Wang, Z. Wu, J. Zhang, T. Xiong, In-situ synthesis of direct solid-state dual Z-scheme WO 3 /g-C 3 N 4 /Bi2O 3 photocatalyst for the degradation of refractory pollutant, *Appl. Catal. B* 227 (2018) 376–385.
- [64] C. Fei, Y. Qi, Z. Yu, H. An, J. Zhao, T. Xie, Q. Xu, X. Li, D. Wang, G. Zeng, Photo-reduction of bromate in drinking water by metallic Ag and reduced graphene oxide (RGO) jointly modified BiVO 4 under visible light irradiation, *Water Res.* 101 (2016) 555–563.
- [65] F. Chen, Q. Yang, J. Sun, F. Yao, S. Wang, Y. Wang, X. Wang, X. Li, C. Niu, D. Wang, Enhanced photocatalytic degradation of tetracycline by AgI/BiVO 4 heterojunction under visible-light irradiation: mineralization efficiency and mechanism, *ACS Appl. Mater. Interfaces* 8 (2016) 32887.
- [66] F. Wang, Y. Wang, Y. Li, X. Cui, Q. Zhang, Z. Xie, H. Liu, Y. Feng, W. Lv, G. Liu, The facile synthesis of a single atom-dispersed silver-modified ultrathin g-C 3 N 4 hybrid for the enhanced visible-light photocatalytic degradation of sulfamethazine with peroxymonosulfate, *Dalton Trans.* 47 (2018) 6924–6933.
- [67] H. Wang, Y. Su, H. Zhao, H. Yu, S. Chen, Y. Zhang, X. Quan, Photocatalytic oxidation of aqueous ammonia using atomic single layer graphitic-C 3 N 4 , *Environ. Sci. Technol.* 48 (2014) 11984–11990.
- [68] G. Zhang, X. Wang, A facile synthesis of covalent carbon nitride photocatalysts by Co-polymerization of urea and phenylurea for hydrogen evolution, *J. Catal.* 307 (2013) 246–253.
- [69] N.O. Gopal, A. Hsinhsia Lo, S.C. Ke, Chemical State and environment of boron dopant in B,N-codoped anatase TiO 2 nanoparticles: an avenue for probing diamagnetic dopants in TiO 2 by electron paramagnetic resonance spectroscopy, *J. Am. Chem. Soc.* 130 (2008) 2760–2761.
- [70] F. Wang, Y. Feng, P. Chen, Y. Wang, Y. Su, Q. Zhang, Y. Zeng, Z. Xie, H. Liu, Y. Liu, W. Lv, G. Liu, Photocatalytic degradation of fluoroquinolone antibiotics using ordered mesoporous g-C 3 N 4 under simulated sunlight irradiation: kinetics, mechanism, and antibacterial activity elimination, *Appl. Catal. B* 227 (2018) 114–122.
- [71] X.J. Wen, C.G. Niu, L. Zhang, C. Liang, G.M. Zeng, A novel Ag 2 O/CeO 2 heterojunction photocatalysts for photocatalytic degradation of enrofloxacin: possible degradation pathways, mineralization activity and an in depth mechanism insight, *Appl. Catal. B* (2018) 221.
- [72] C. Jiang, Y. Ji, Y. Shi, J. Chen, T. Cai, Sulfate radical-based oxidation of fluorquinolone antibiotics: kinetics, mechanisms and effects of natural water matrices, *Water Res.* 106 (2016) 507.
- [73] C. Wang, L. Yin, Z. Xu, J. Niu, L.-A. Hou, Electrochemical degradation of enrofloxacin by lead dioxide anode: kinetics, mechanism and toxicity evaluation, *Chem. Eng. J.* 326 (2017) 911–920.
- [74] Y. Ide, F. Liu, J. Zhang, N. Kawamoto, K. Komaguchi, Y. Bando, D. Golberg, Hybridization of Au nanoparticle-loaded TiO 2 with BN nanosheets for efficient solar-driven photocatalysis, *J. Mater. Chem. A* 2 (2014) 4150–4156.
- [75] P. Chen, F. Wang, Z.F. Chen, Q. Zhang, Y. Su, L. Shen, K. Yao, Y. Liu, Z. Cai, W. Lv, Study on the photocatalytic mechanism and detoxicity of gemfibrozil by a sunlight-driven TiO 2 /carbon dots photocatalyst: the significant roles of reactive oxygen species, *Appl. Catal. B* 204 (2017) 250–259.
- [76] Q. Liu, T. Chen, Y. Guo, Z. Zhang, X. Fang, Ultrathin g-C 3 N 4 nanosheets coupled with carbon nanodots as 2D/0D composites for efficient photocatalytic H 2 evolution, *Appl. Catal. B* 193 (2016) 248–258.
- [77] M.Y. Ye, Z.H. Zhao, Z.F. Hu, L.Q. Liu, H.M. Ji, Z.R. Shen, T.Y. Ma, 0D/2D heterojunctions of vanadate quantum dots/graphitic carbon nitride nanosheets for enhanced visible-light-driven photocatalysis, *Angew. Chemie* 129 (2017) 8407–8411.
- [78] M.Q. Yang, Y.J. Xu, W. Lu, K. Zeng, H. Zhu, Q.H. Xu, G.W. Ho, Self-surface charge exfoliation and electrostatically coordinated 2D hetero-layered hybrids, *Nat. Commun.* 8 (2017) 14224.
- [79] W. Liu, L. Cao, W. Cheng, Y. Cao, X. Liu, W. Zhang, X. Mou, L. Jin, X. Zheng, W. Che, Single-site active cobalt-based photocatalyst with a long carrier lifetime for spontaneous overall water splitting, *Angew. Chemie* 56 (2017) 9312.
- [80] R. Shi, H.F. Ye, F. Liang, Z. Wang, K. Li, Y. Weng, Z. Lin, W.F. Fu, C.M. Che, Y. Chen, Interstitial P-doped CdS with long-lived photogenerated electrons for photocatalytic water splitting without sacrificial agents, *Adv. Mater.* (2017) 1705941.